A Dual-Band Dual-Sense Circularly Polarized Rectenna for Millimeter-Wave Power Transmission

Yan Wang, Haoyuan Pan, *Member, IEEE*, and Tse-Tin Chan, *Member, IEEE*

***Abstract*—This paper puts forth a novel dual-band dual-sense (DBDS) circularly polarized (CP) rectenna operating at 24 GHz and 28 GHz for millimeter-wave power transmission (MMPT). An arc-shaped parasitic patch is loaded near a single-layer circular patch to induce chirality. The chiral structure transforms linearly polarized (LP) waves, coupled from a slot, into left-hand CP (LHCP) and right-hand CP (RHCP) waves at the two respective operating frequencies. The DBDS CP antenna array, consisting of four antenna elements, each integrated with a substrate-integrated waveguide (SIW) cavity, achieves gains of 17.1 dBic and 17.0 dBic at 24 GHz and 28 GHz, respectively. A dual-band rectifying circuit, comprising two L-section impedance transformers and three fan-shaped low-pass filters, is designed and integrated with the antenna array to form the DBDS CP rectenna. The proposed rectenna achieves maximum conversion efficiencies of 49.1% and 47.8% at 24 GHz and 28 GHz, respectively, both at an input power of 18 dBm. The compact structure and low profile make it suitable for large-scale array applications in MMPT systems.**

***Index Terms*—Chirality, circular polarization, dual-band dual-sense, millimeter wave, rectenna, wireless power transmission.**

I. Introduction

MILLIMETER-WAVE power transmission (MMPT) offers numerous advantages, including compact size and large absolute bandwidth, making it suitable for diverse applications such as Internet of Things (IoT) sensor networks, microrobots, drones, and solar satellites [1]. A rectenna, a key component of wireless power transmission systems, captures electromagnetic wave energy and converts it into direct current (DC) [2].

Circularly polarized (CP) antennas have significant advantages over linearly polarized (LP) antennas in reducing polarization mismatch losses and suppressing multipath interference. In MMPT systems, CP rectennas can receive any polarized wave except for CP waves with orthogonal rotation, thereby reducing microwave energy loss due to polarization misalignment. For instance, in 2014, [3] designed a substrate-integrated waveguide (SIW) CP rectenna, achieving CP operation by diagonally slotting a circular patch. The design achieved a gain of 12.6 dBic by incorporating the SIW cavity and array configuration, along with a conversion efficiency (CE) of 42% at an input power of 12.6 dBm. In 2016, [4] designed a CP rectenna using a Fabry-Pérot resonant cavity antenna fed by a cut-corner rectangular patch CP antenna, loaded with a polarization-insensitive superstrate, achieving a gain of 20 dBic and a CE of 63.8% at an input power of 18.9 dBm. However, this structure included a thick air layer of 0.54λ between the feed antenna and the superstrate, increasing the antenna profile and complicating the design. More recently, [5] designed a metamaterial-based CP rectenna, achieving CP operation through cross-feeding slots of different lengths. By loading metallic perforations, they obtained a gain of 11.3 dBic and a CE of 63% at an input power of 15.2 dBm. Despite these advancements, single-band millimeter-wave (MMW) CP rectennas generally suffer from relatively low receiving antenna gains or limited bandwidth.

Multiband rectennas, capable of capturing microwave energy across multiple frequency bands, can address this limitation. For example, in 2010, [6] designed a 35/94 GHz dual-band rectenna to enable simultaneous rectification in two frequency bands with low atmospheric attenuation. The rectenna was designed in a CMOS process, comprising a linear tapered slot antenna, a slotline to finite-width ground coplanar waveguide transition, and a full-wave rectifying circuit, achieving CEs of 53% and 37% at the two frequencies, respectively, for a power density of 30 mW/cm^2. In 2020, [7] designed a triple-frequency rectifying circuit for an MMPT system operating at 24 GHz, 28 GHz, and 38 GHz, achieving rectifying efficiencies of 44%, 41.3%, and 39.7%, respectively, at an input power of 17.5 dBm. Nevertheless, the integration of CP properties with dual-band or multiband rectification in MMW rectennas remains underexplored.

At lower frequency bands, the design methods and theoretical analyses of rectennas are relatively mature, with numerous studies on CP rectennas [1], [2], [8], multiband rectifying circuits [9], and multiband rectennas [1], [2], [10]. Several studies have explored integrating CP with dual-band performance, such as [11], [12]. Dual-band dual-sense (DBDS) CP rectennas can further reduce energy loss due to polarization mismatch between transmitting and receiving antennas while simultaneously harvesting energy from multiple frequencies to generate more DC power. A DBDS CP rectenna consists of a DBDS CP receiving antenna and a dual-band or wideband rectifying circuit covering the operating frequencies.

DBDS CP antennas need to produce +90° and -90° phase differences in the two bands. A straightforward method for achieving DBDS CP operation is direct integration, where two radiating elements with different bands and CP rotation directions are arranged either horizontally [13] or stacked

This work was supported in part by the National Natural Science Foundation of China under Grant 62371302 and in part by the Research Matching Grant Scheme from the Research Grants Council of Hong Kong. *(Corresponding author: Tse-Tin Chan.)*

Y. Wang and T.-T. Chan are with the Department of Mathematics and Information Technology, The Education University of Hong Kong, Hong Kong SAR, China (e-mails: wangyan@eduhk.hk, tsetinchan@eduhk.hk).

H. Pan is with the College of Computer Science and Software Engineering, Shenzhen University, Shenzhen, 518060, China (e-mail: hypan@szu.edu.cn).

vertically [14]. However, this approach increases the antenna size or profile. Alternatively, dual-band orthogonal modes or dual-band feed networks can be designed. For example, [15] proposed a four-element square patch array that excites two pairs of orthogonal degenerate modes, TM_{10}/TM_{01} and TM_{30}/TM_{03}, with different branches to achieve left-hand CP (LHCP) and right-hand CP (RHCP) operation at 2.53 GHz and 3.59 GHz, respectively. However, the 3-dB axial ratio (AR) bandwidths were only 0.67% and 0.6%, respectively. Similarly, [16] designed a dual-band branch-line coupler to generate +90° and -90° phase differences at 0.92 GHz and 2.45 GHz, respectively. The 3 dB AR bandwidths at these frequencies were 4.4% and 8.2%, respectively, but the feed network was complex. Note that these DBDS CP antennas often feature complex radiating structures or feed networks, making them difficult to miniaturize and integrate into arrays as the operating frequency increases.

Chiral structures, characterized by their inability to be superimposed on their mirror images and the absence of any plane of symmetry, emerge as a potential solution [17]. Chiral structures can rotate the polarization plane of an LP wave as it passes through and can operate at two distinct frequency bands, including opposite circular rotations (LHCP and RHCP), due to their bidirectional anisotropy with respect to electromagnetic waves. Some studies have applied chiral structures to single or dual circular polarizers and supersurfaces. For example, [18] and [19] proposed a DBDS CP horn antenna and a Fabry–Pérot resonator antenna, respectively. These designs consisted of an LP feed antenna and a chiral superstrate with a double-layer structure, resulting in large sizes and high profiles. In our previous work [20], an MMW DBDS CP antenna utilizing a chiral structure was designed, achieving gains of 6.9 dBic with LHCP operation and 7.1 dBic with RHCP operation at 24 GHz and 28 GHz, respectively.

Despite these advancements, the potential of DBDS CP rectennas in the MMW band has not been fully explored. Compared to lower-frequency rectenna designs, achieving precise diode input impedance matching and designing high-gain antennas with further miniaturization and scalability for larger applications are more challenging at millimeter-wave frequencies. Due to factors such as higher propagation losses, shorter wavelengths, and stricter fabrication tolerances, efficient impedance matching and miniaturization become more difficult at these frequencies.

To address these challenges, this paper proposes the first DBDS CP rectenna design for MMPT applications. The main contributions of this work are as follows:

- **Design of a Dual-Band Dual-Sense CP MMW Rectenna:** The proposed MMW rectenna supports dual bands (24 GHz and 28 GHz) and dual-sense circular polarization (LHCP at 24 GHz and RHCP at 28 GHz). This combination enhances power reception efficiency and reduces polarization mismatch, making it highly suitable for MMPT applications such as IoT systems and 6G communications.
- **Chirality-Based, High-Gain, and Compact Antenna Design:** Building upon our previous work [20], the antenna achieves dual-sense CP operation with a simple single-layer design by introducing an arc-shaped parasitic patch near a circular patch to form a chiral structure. In this work, further integration with SIW cavities and an array configuration enables the receiving antenna array to achieve high gains of 17.1 dBic at 24 GHz and 17.0 dBic at 28 GHz, while maintaining a compact form factor that is scalable for larger applications.
- **Efficient Dual-Band Rectifying Circuit:** A 24/28 GHz dual-band rectifying circuit is designed, comprising two L-section impedance transformers and three fan-shaped low-pass filters to enable impedance matching and harmonic suppression while eliminating the need for lumped components. Integrating the rectifying circuit with the antenna array forms a compact and efficient DBDS CP rectenna suitable for MMPT systems, achieving conversion efficiencies of 49.1% at 24 GHz and 47.8% at 28 GHz, both at an input power of 18 dBm.

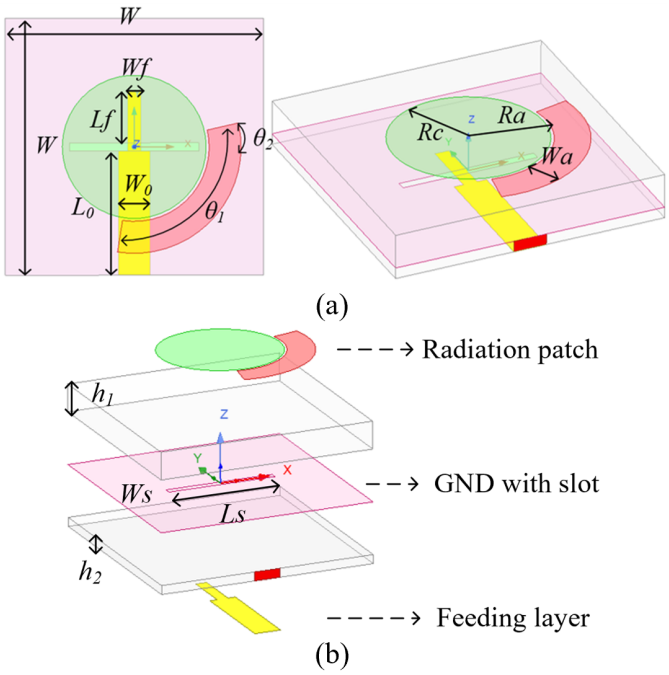

Fig. 1. Structure of the antenna element: (a) top view and (b) perspective view.

The rest of this paper is organized as follows. Section II details the DBDS CP receiving antenna design. Section III presents the dual-band rectifying circuit design. Section IV describes the integration of the DBDS CP rectenna and presents the experimental results of the fabricated prototype. Finally, Section V concludes this paper.

II. DBDS CP Receiving Antenna Design

A. Antenna Element Structure

This section presents a DBDS CP antenna based on a chiral structure operating at 24 GHz and 28 GHz, as shown in Fig. 1. The antenna element is composed of two substrates and three metal layers. The substrates are Rogers RT/duroid 5880 with a relative dielectric constant ε_r of 2.2, a loss tangent of 0.0009, and thicknesses h_1 and h_2 for the upper and lower

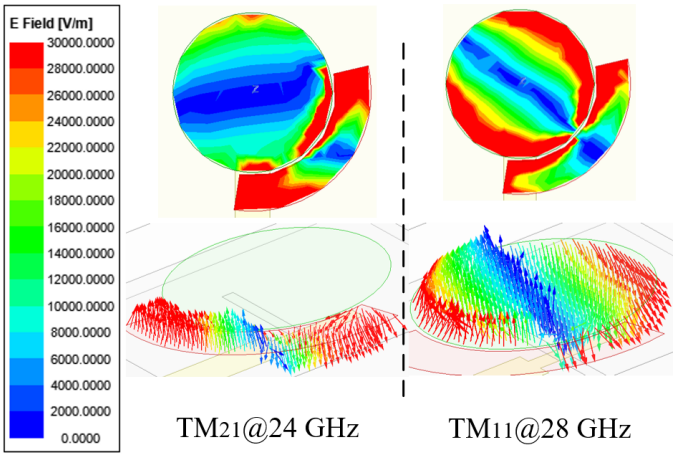

Fig. 2. Electric field distributions of the antenna element.

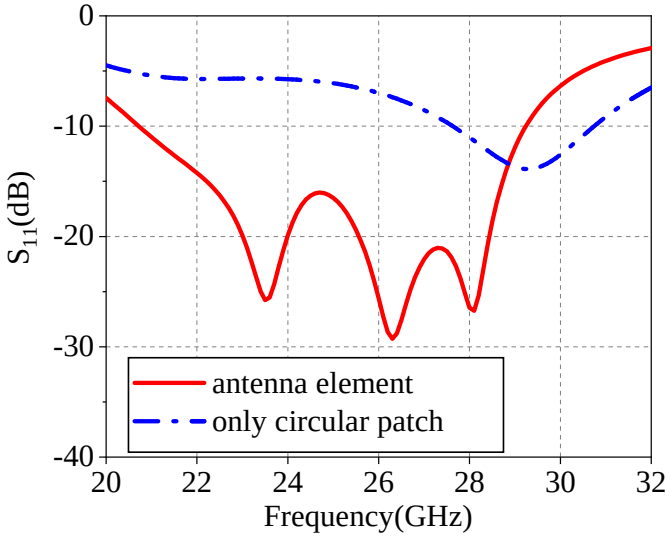

Fig. 3. Simulated reflection coefficient S_{11} of the antenna element.

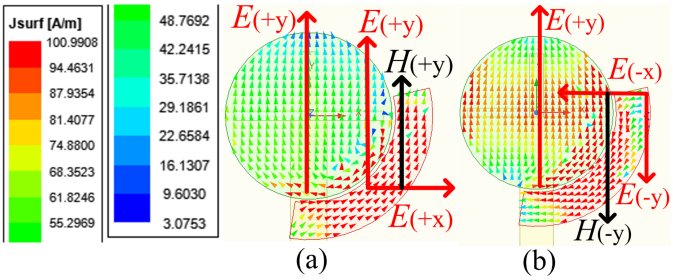

Fig. 4. Surface current distribution of the antenna element at (a) 24 GHz and (b) 28 GHz.

layers, respectively. The chiral structure is composed of a circular patch with a radius of R_c and an arc-shaped parasitic patch with a radius of R_a, width of W_a, central angle of θ_1, and deviation angle from the x-axis of θ_2. The distance between the circular patch and the arc-shaped patch is 0.1 mm, forming a capacitive arc-shaped gap that induces electric field coupling between the two patches, which influences the antenna's resonant behavior. The feeding layer consists of a 50 Ω microstrip line and an impedance matching branch with a length of L_f and width of W_f.

B. Operation Principle

1) Dual-Band Operation Principle: The dual-band operation is achieved by combining the resonant modes of the circular patch and the arc-shaped parasitic patch. The electric field distributions of the antenna element at the two operating frequencies are shown in Fig. 2. The lower band resonance is primarily generated by the TM_{21} mode of the arc-shaped patch, while the upper band resonance is generated by the TM_{11} mode of the circular patch.

When the lower band resonates, electromagnetic energy is coupled to the radiation patch through the rectangular slot and then fed into the arc-shaped patch via the capacitive arc-shaped gap. The electric field concentrates at both ends of the arc-shaped patch, behaving similarly to a quarter-ring patch. The electric field distribution on the arc-shaped patch corresponds to the TM_{21} mode excited by a ring patch.

In contrast, when the upper band resonates, electromagnetic energy is primarily coupled directly to the circular patch from the rectangular slot. The electric field distribution on the circular patch conforms to the TM_{11} mode. The resonance frequencies of the arc-shaped and circular patches can be approximated according to (1) [21] and (2) [22], respectively, as follows:

$$f(arc) = \frac{c\chi'_{21}}{2\pi R_a\sqrt{\varepsilon_r}},\ \chi'_{21} = 1.61, \tag{1}$$

$$f(circle) = \frac{c\chi'_{11}}{2\pi R_c\sqrt{\varepsilon_r}},\ \chi'_{11} = 1.84, \tag{2}$$

where c is the speed of light in vacuum.

The simulated reflection coefficient of the antenna element is shown in Fig. 3. When only the circular patch is excited, a resonance occurs in the upper band. Incorporating the arc-shaped patch introduces the lower band resonance, and the coupling effect of the capacitive arc-shaped gap causes the upper band resonance to shift downward, resulting in a mid-band resonance. The final antenna element exhibits a reflection coefficient of less than -15 dB within the frequency range of 22.3–28.7 GHz.

2) Dual-Sense CP Principle: The arc-shaped patch breaks the central symmetry of the circular patch, making the patch chiral. When an electromagnetic wave passes through the arc-shaped patch, cross-coupling between the magnetic and electric fields occurs, characterized by the following constitutive relationship:

$$\begin{pmatrix}\overline{D}\\ \overline{B}\end{pmatrix} = \begin{pmatrix}\varepsilon_0\varepsilon_r & i\kappa/c\\ -i\kappa/c & \mu_0\mu_r\end{pmatrix}\begin{pmatrix}\overline{E}\\ \overline{H}\end{pmatrix}, \tag{3}$$

where $\varepsilon_0\varepsilon_r$, $i\kappa/c$, $-i\kappa/c$, and $\mu_0\mu_r$ are scalar constitutive parameters, indicating that the chirality is bi-isotropic. The chirality parameter κ characterizes the strength of the cross-coupling between the magnetic and electric fields. Electric and magnetic currents exist simultaneously, appearing in parallel or antiparallel directions.

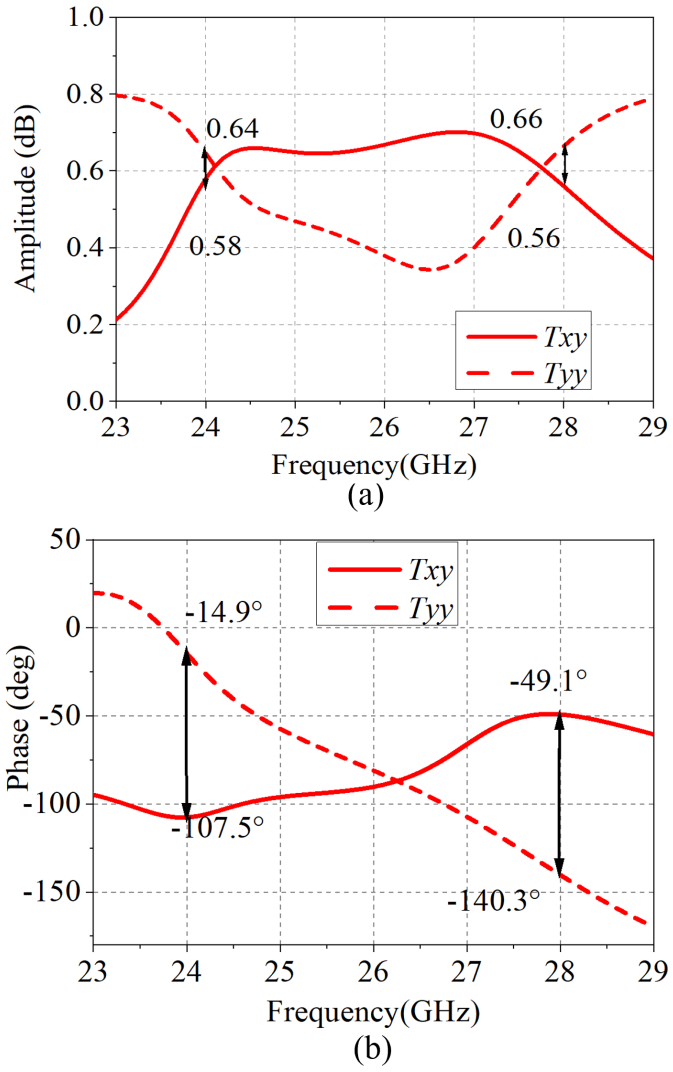

Fig. 5. Frequency response curves for the (a) amplitude and (b) phase.

Fig. 4 depicts the surface current distributions of the antenna when a y-polarized wave passes through the chiral structure. At 24 GHz, the surface current on the circular patch flows in the +y direction, while that on the arc-shaped patch circulates counterclockwise, equivalent to the +y and +x directions. This generates a magnetic field H_y parallel to the electric field E_y. At 28 GHz, the surface current on the arc-shaped patch circulates clockwise, resulting in H_y being antiparallel to E_y. This behavior aligns with (3), where at 24 GHz, the radiation effect is equivalent to a magnetoelectric dipole in the parallel direction, and at 28 GHz, it is equivalent to a magnetoelectric dipole in the antiparallel direction. These magnetoelectric dipoles in the parallel and antiparallel directions produce -90° and +90° phase differences, respectively, for the DBDS CP antenna.

When a y-polarized wave is incident on the proposed chiral structure through the rectangular slot, the transmitted electric field can be expressed as:

$$\overline{E} = \left(T_{xy}\vec{x} \pm T_{yy}\vec{y}\right) E_0, \tag{4}$$

where T_{xy} and T_{yy} are the transmittances of the x- and y-polarized components in the transmitted field, respectively, and E_0 is the amplitude of the incident field. The simulated values of T_{xy} and T_{yy} are depicted in Fig. 5. The magnitude ratios $|T_{xy}| / |T_{yy}|$ are 1.1 at 24 GHz and 1.18 at 28 GHz. Moreover, the phase differences $\phi(T_{xy}) - \phi(T_{yy})$ are -92.5° at 24 GHz and 91.2° at 28 GHz. Consequently, the polarization plane of the LP wave is transformed into LHCP and RHCP waves at 24 GHz and 28 GHz, respectively, as it passes through the proposed chiral structure. For a more comprehensive description of the proposed antenna elements, please refer to our previous work [20].

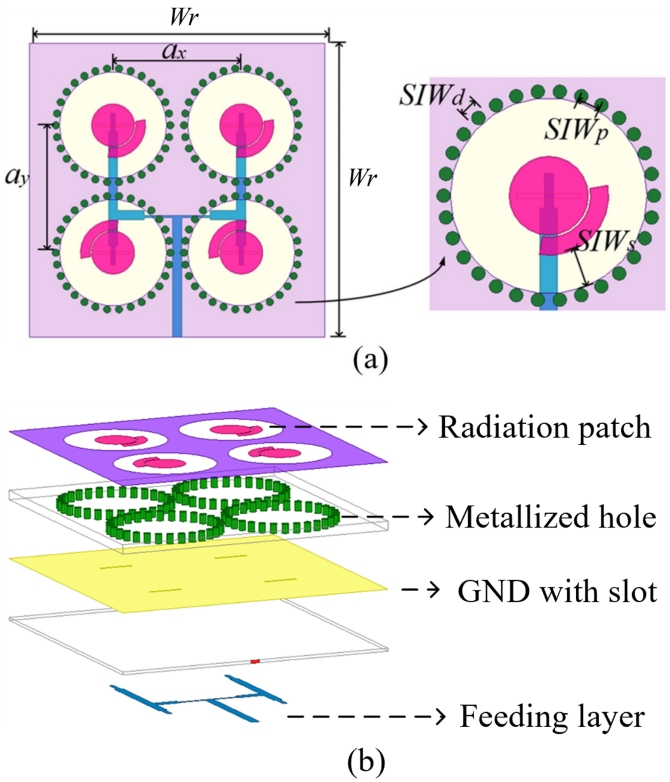

Fig. 6. Structure of the antenna array: (a) top view and (b) perspective view.

TABLE I
PARAMETERS OF THE RECEIVING ANTENNA ARRAY

Parameter	W	R_c	R_a	W_a	L_f	L_0
Length (mm)	6.85	1.7	1.85	0.75	1.65	2.8
Parameter	W_f	W_0	L_s	W_s	W_r	a_x
Length (mm)	0.34	0.75	2.7	0.2	24	10.4
Parameter	a_y	SIW_d	SIW_p	SIW_s	h_1	h_2
Length (mm)	10.4	0.6	1.1	1.6	0.79	0.254
Parameter	θ_1	θ_2				
Deg (°)	110	-16				

C. Four-Element Receiving Antenna Array

To achieve a high-gain receiving antenna, a four-element SIW antenna array is designed in this paper, as shown in Fig. 6. The upper and lower antenna elements are connected directly through a microstrip feeding line in equal-amplitude reverse-phase mode, while the left and right 1 × 2 arrays are connected through a power divider in an equal-amplitude mode

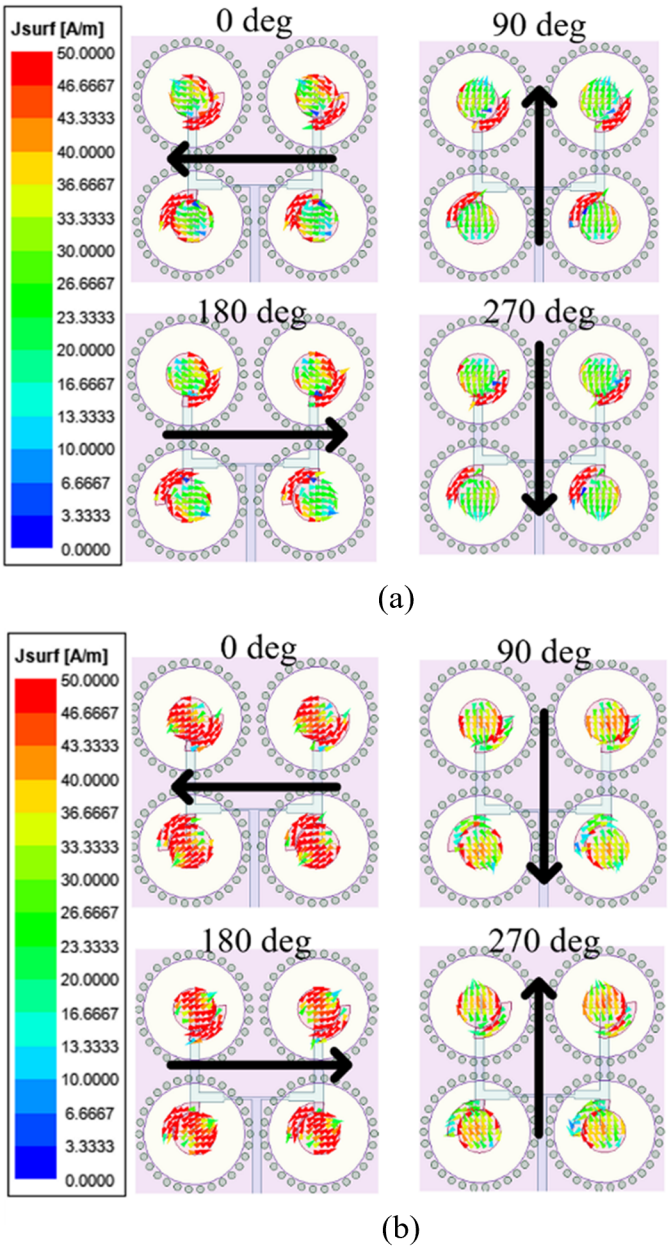

Fig. 7. Surface current distribution of the receiving antenna array at (a) 24 GHz and (b) 28 GHz.

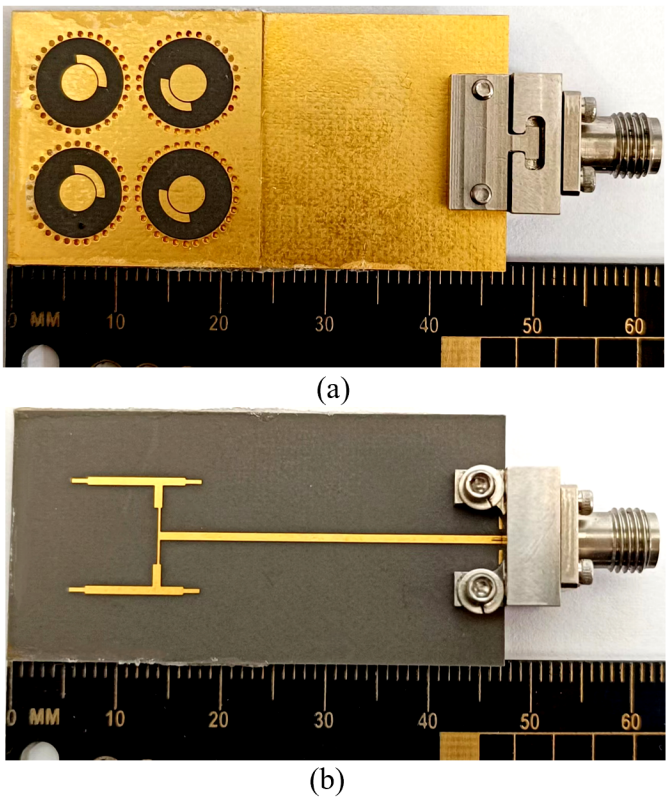

Fig. 8. Photographs of the receiving antenna: (a) front view and (b) back view.

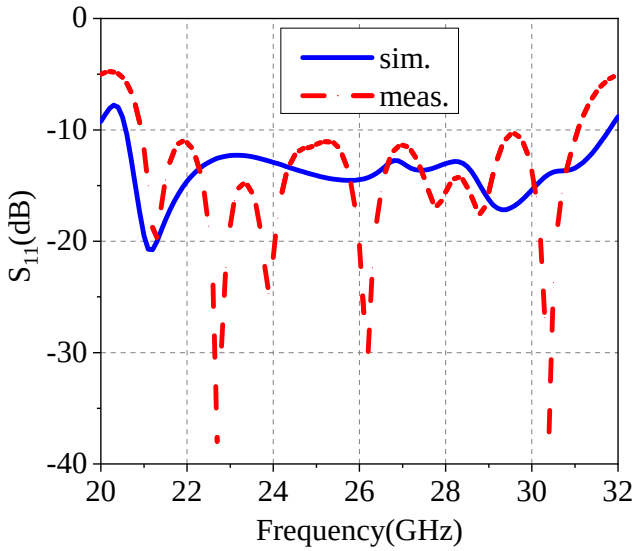

Fig. 9. Simulated (sim.) and measured (meas.) reflection coefficients S_{11} of the receiving antenna.

[23]. Due to the opposite feeding directions of the upper and lower feeding lines and the 180° phase difference introduced by the different lengths of the feeding lines, the lower two elements are oriented in reverse relative to the upper elements. This configuration ensures that the far-field electric fields of all the elements are aligned in the same direction, thereby increasing the overall antenna gain.

The element spacing within this equal-amplitude, in-phase patch array is $0.8\lambda_0$, where λ_0 is the free-space wavelength at 24 GHz. This spacing maximizes gain and prevents grating lobes. Each antenna element in the array is integrated with a circular SIW cavity, which helps confine electromagnetic energy, reduces surface wave dispersion in the medium, and improves antenna gain. By loading the circular SIW cavity, the gain increases by at least 2 dB at both 24 GHz and 28 GHz. The parameters of the receiving antenna array are summarized in Table I.

Fig. 7 shows the surface current distributions of the receiving antenna array at different phases. At 24 GHz, the currents circulate clockwise, indicating LHCP operation, while at 28 GHz, the currents circulate counterclockwise, indicating

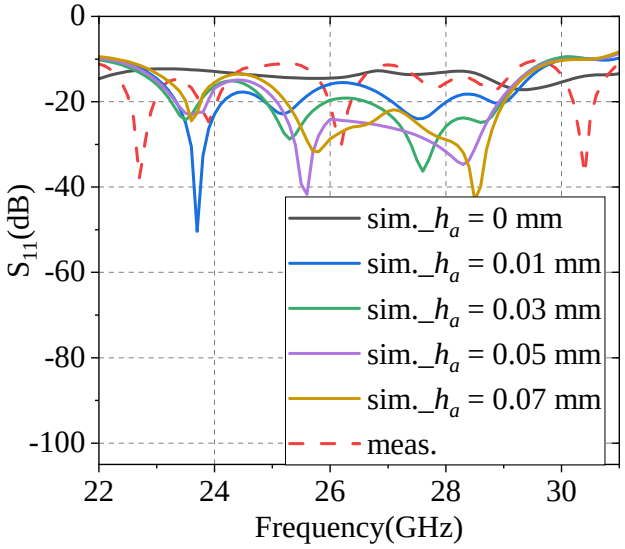

Fig. 10. Simulated (sim.) and measured (meas.) reflection coefficients S_{11} of the receiving antenna under various air layer thicknesses h_a.

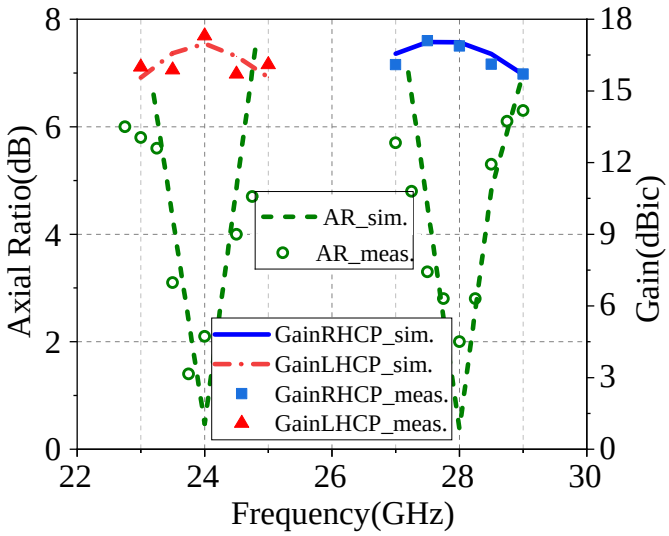

Fig. 11. Simulated (sim.) and measured (meas.) 3-dB AR bandwidth and gain of the receiving antenna.

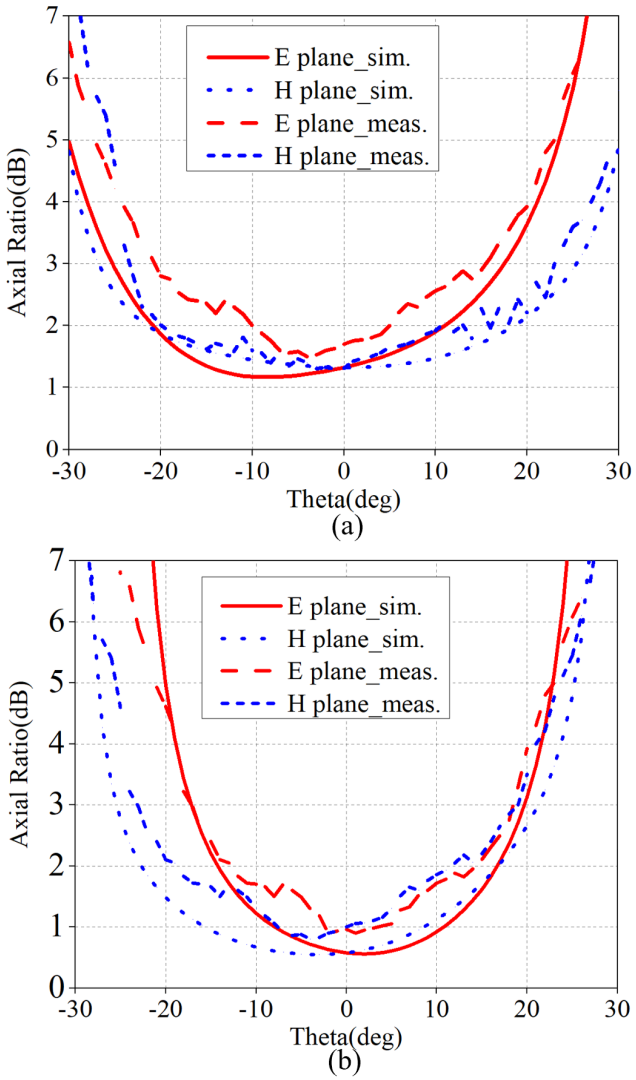

Fig. 12. Simulated (sim.) and measured (meas.) 3-dB AR beam width of the receiving antenna at (a) 24 GHz and (b) 28 GHz.

RHCP operation.

D. Simulation and Measurement of the Receiving Antenna

Photographs of the fabricated antenna are shown in Fig. 8. To accommodate the terminal connector during measurement and reduce its impact, the ground is extended by approximately one wavelength in free space.

The reflection coefficient results are shown in Fig. 9. The measured impedance bandwidth is 38.5% (21–31 GHz), which covers both operating frequencies. Since the designed antenna is composed of two substrates, an unintended thin air layer was introduced during assembly. To analyze the discrepancies between the simulated and measured results, the reflection coefficients of the receiving antenna under various air layer thicknesses h_a are simulated, as shown in Fig. 10. It can be observed that as h_a changes from 0.01 mm to 0.07 mm, several resonances are excited within the bandwidth range, similar to the measured results. Therefore, the discrepancies between the simulated and measured reflection coefficient results are mainly attributed to the tiny air layer introduced during the assembly of the two substrates, as well as fabrication tolerances and measurement inaccuracies.

The 3-dB axial ratio (AR) bandwidth and gain results are shown in Fig. 11. The measured 3-dB AR bandwidths are 2.1% (23.7–24.2 GHz) in the lower band and 1.8% (27.7–28.2 GHz) in the upper band. LHCP operation is achieved in the lower band with a peak gain of 17.1 dBic at 24 GHz, and RHCP operation is achieved in the upper band with a peak gain of 17.0 dBic at 28 GHz.

The 3-dB AR beam width results are shown in Fig. 12. The measured 3-dB AR beam widths at 24 GHz are 42.7° (E-plane) and 52.1° (H-plane), and at 28 GHz, they are 46.6° (xoz-plane) and 36.8° (yoz-plane).

In addition, the radiation pattern results are shown in

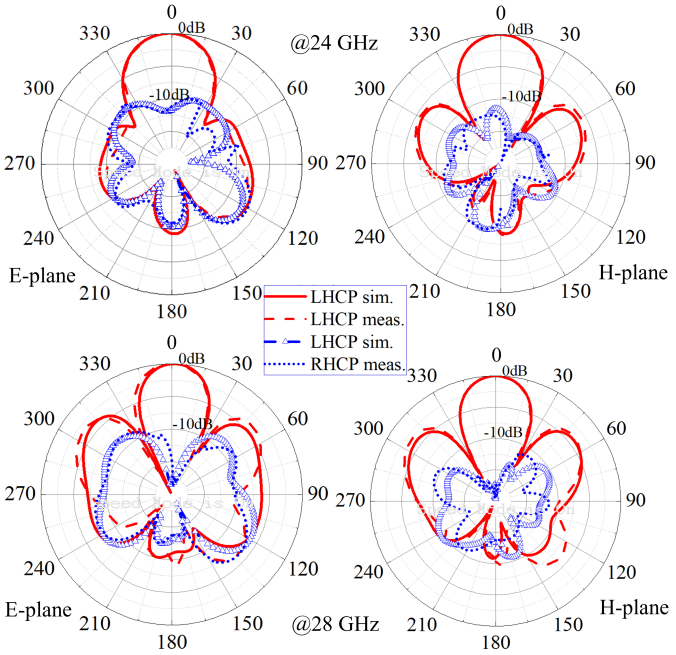

Fig. 13. Simulated (sim.) and measured (meas.) normalized radiation patterns of the receiving antenna.

Fig. 13. At 24 GHz, the half-power beam widths (HPBWs) in the E- and H-planes are 32.3° and 30.3°, respectively, while at 28 GHz, the HPBWs are 25.5° and 26.4°, respectively. The cross-polarization levels are below -22.4 dB and -29.6 dB, respectively, indicating excellent polarization purity. The radiation efficiency of the receiving antenna array, simulated using the high-frequency structure simulator (HFSS) software, is 99.0% at 24 GHz and 99.7% at 28 GHz.

III. Dual-Band Rectifying Circuit Design

A. Rectifying Circuit Structure

This section details the 24/28 GHz dual-band rectifying circuit design proposed in this paper. A commercial Schottky diode (MA4E1317) is utilized in the rectifying circuit, characterized by a zero-bias junction capacitance C_j of 0.02 pF, a series resistance Rs of 4 Ω, a reverse breakdown voltage V_{br} of 7 V, a forward conduction voltage V_{bi} of 0.7 V, and an operational frequency up to 80 GHz. Before designing the rectifying circuit, it is essential to obtain the diode input impedance (DII). However, in the MMW band, theoretical formulas for DII can exhibit significant errors. Hence, we employ an experimental method to obtain the DII [23].

The available power for the rectifying circuit and rectenna depends on the characteristics of the diode. The diode starts to conduct effectively when the voltage across it exceeds its forward voltage at a certain input power. Below this threshold input power (approximately 0 dBm in our design), the diode does not conduct effectively, resulting in negligible or zero rectifying efficiency. As the input power increases beyond 0 dBm, the diode conducts more effectively. However, if the input power exceeds 20 dBm, there is a risk of damaging the diode due to exceeding its input power limitations. Therefore, the operational input power range for our design is from 0 dBm to 20 dBm, making it suitable for power transmission applications rather than low-power environmental energy harvesting, which typically operates at input power levels below 0 dBm.

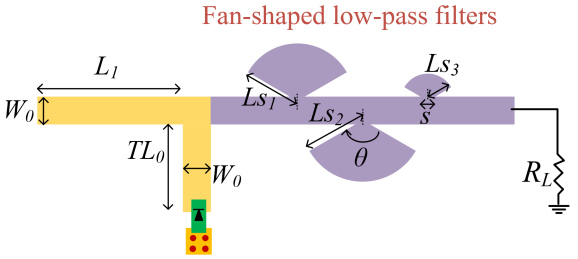

Fig. 14. Structure of the rectifying circuit for measuring diode input impedance.

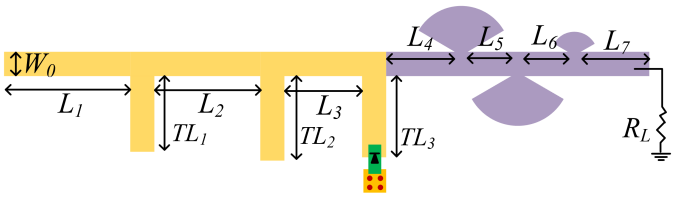

Fig. 15. Structure of the proposed rectifying circuit, where the three fan-shaped low-pass filters are identical to those in Fig. 14.

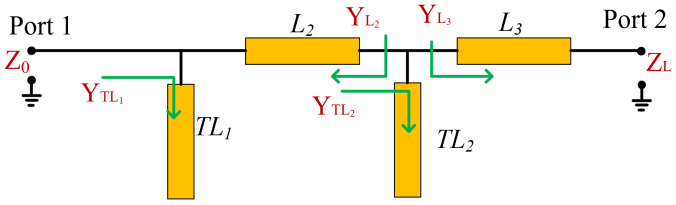

Fig. 16. Impedance matching network of the rectifying circuit.

TABLE II
Parameters of the Rectifying Circuit

Parameter	L_1	L_2	L_3	L_4	L_5
Length (mm)	3.9	3.3	2.4	1.95	1.37
Parameter	L_6	L_7	TL_1	TL_2	TL_3
Length (mm)	1.49	2.87	2.63	2.9	2.75
Parameter	L_{s1}	L_{s2}	L_{s3}	s	W_0
Length (mm)	1.35	1.49	1.24	0.4	0.75

We fabricate a rectifying circuit without a matching network and measure the diode input impedance using a vector network analyzer (VNA). The structure of the rectifying circuit used for DII measurement is shown in Fig. 14. It consists of a microstrip line of length L_1 and width W_0, an open microstrip branch of length TL_0 and width W_0, and three fan-shaped low-pass filters. The three filters each have a central angle of θ = 120°, a width of s embedded in the microstrip line, and different radii of L_{s1}, L_{s2}, and L_{s3}. The length L_1 is set to $\lambda_0/2$ so that the input port impedance equals the diode input impedance. The open microstrip branch with a specific length TL_0 is used to eliminate the imaginary part of the diode input impedance at the operating frequencies.

The three fan-shaped low-pass filters in the rectifying circuit, with relatively small physical dimensions, are simple and

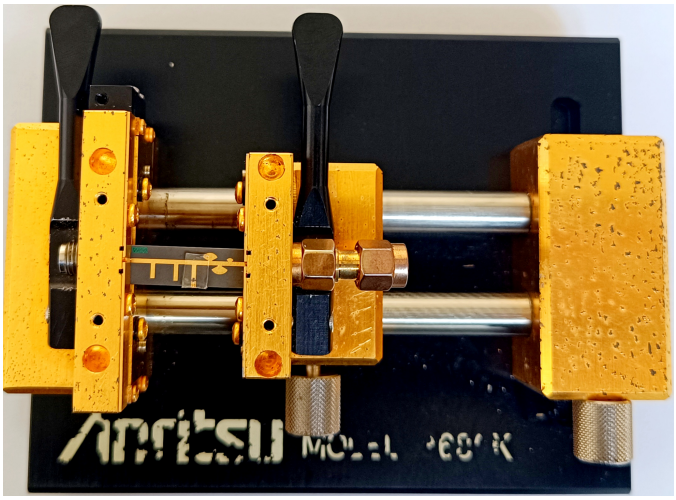

Fig. 17. Photograph of the fabricated rectifying circuit with the fixture.

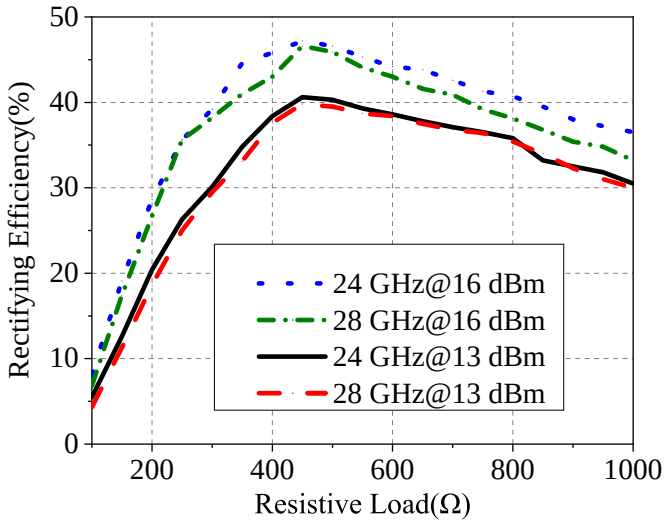

Fig. 18. Measured rectifying efficiency of the rectifying circuit versus the resistive load under different input powers.

easy to adjust. They are used to suppress unwanted signals at specific frequencies in combination with microstrip lines. Specifically, the fan-shaped low-pass filter with a radius of L_{s2} suppresses the unwanted fundamental frequencies at 24 GHz and 28 GHz, while the filters with radii of L_{s1} and L_{s3} suppress the second harmonic frequencies at 48 GHz and 56 GHz, respectively. The three filters are simulated using Agilent Advanced Design System (ADS), showing reflection coefficients close to 0 dB and insertion losses greater than 15 dB over the frequency range of 21 GHz to 58 GHz, ensuring effective suppression of both fundamental and second harmonic frequencies.

Using this setup, the diode input impedance is measured to be 35 Ω with a load R_L of 450 Ω at 24 GHz and 31 Ω with the same load at 28 GHz.

Based on the measured diode input impedance, we design a 24/28 GHz dual-band rectifying circuit. Fig. 15 shows the structure of the proposed rectifying circuit. It consists of a microstrip line of length L_1, two open microstrip branches of lengths TL_1 and TL_2, two series branches of lengths L_2 and L_3, an open microstrip branch of length TL_3 connected to a shunt diode, and three fan-shaped low-pass filters. The width of the microstrip lines and branches is W_0.

The diode input impedance is transformed to the receiving antenna's common impedance of 50 Ω using two L-section impedance transformers composed of an open microstrip branch of length TL_1 (TL_2) and a series branch of length L_2 (L_3). The three fan-shaped low-pass filters are the same as those used in the rectifying circuit for DII measurement. The diode is grounded through four metalized via holes, and the output DC voltage is measured across the load R_L. The parameters of the rectifying circuit are listed in Table II.

To achieve dual-band impedance matching at 24 GHz and 28 GHz, we design an impedance matching network (IMN) as shown in Fig. 16. The IMN consists of two L-section impedance transformers. The matching conditions are established by ensuring that the admittances at the common node of the L-section network are conjugate-matched, satisfying the following equations:

$$Y_{L_3}(f_1) = Y^*_{L_3}(f_2), \tag{5}$$

$$Y_{TL_2}(f_1) = Y^*_{TL_2}(f_2), \tag{6}$$

$$Y_{L_2}(f_1) = Y^*_{L_2}(f_2), \tag{7}$$

where f_1 and f_2 represent the two operating frequencies of 24 GHz and 28 GHz, respectively, and Y^* denotes the complex conjugate of the admittance Y. The open microstrip branch of length TL_1 has a characteristic impedance of Z_0 (receiving antenna impedance), and it does not alter the matching at 24 GHz and 28 GHz.

B. Measurement of the Rectifying Circuit

The rectifying circuit is simulated using electromagnetic (EM) analysis and harmonic balance (HB) simulations in Agilent ADS. The circuit is fabricated and loaded on a fixture, as shown in Fig. 17. The physical dimensions are 20.7 mm × 6.7 mm × 0.254 mm. The rectifying efficiency (RE) of the rectifying circuit is calculated as:

$$\eta_{RE} = \frac{V_{dc}^2}{R_L P_{in,c}} \times 100\%, \tag{8}$$

where V_{dc} is the DC voltage across the load, R_L is the resistive load, and $P_{in,c}$ is the input power to the rectifying circuit.

The measured RE of the rectifying circuit versus the resistive load under different input power levels is shown in Fig. 18. At 24 GHz, when the input power to the rectifying circuit is 13 dBm and 16 dBm, the RE is 40.6% and 47.2%, respectively, with the highest efficiency at $R_L = 450$ Ω. Similarly, at 28 GHz, the RE is 39.8% and 46.6% under the same input powers, with the highest efficiency also at $R_L = 450$ Ω. These results indicate that the optimal load resistance is 450 Ω.

The measured RE and the output DC voltage of the rectifying circuit versus the frequency with a 450 Ω resistive load are shown in Fig. 19. In the frequency range of 22 GHz to 24 GHz, both the RE and the output DC voltage increase with

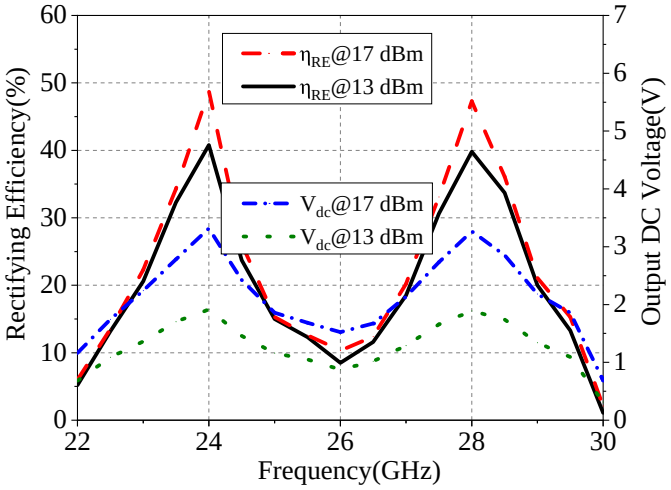

Fig. 19. Measured rectifying efficiency and output DC voltage of the rectifying circuit versus frequency under different input powers.

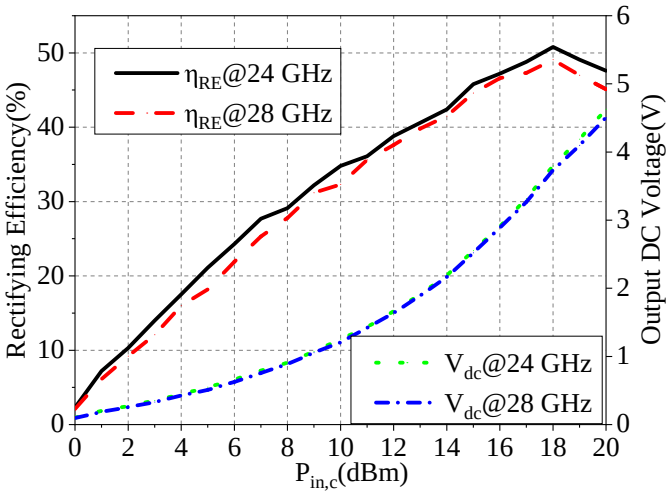

Fig. 20. Measured rectifying efficiency and output DC voltage of the rectifying circuit versus input power.

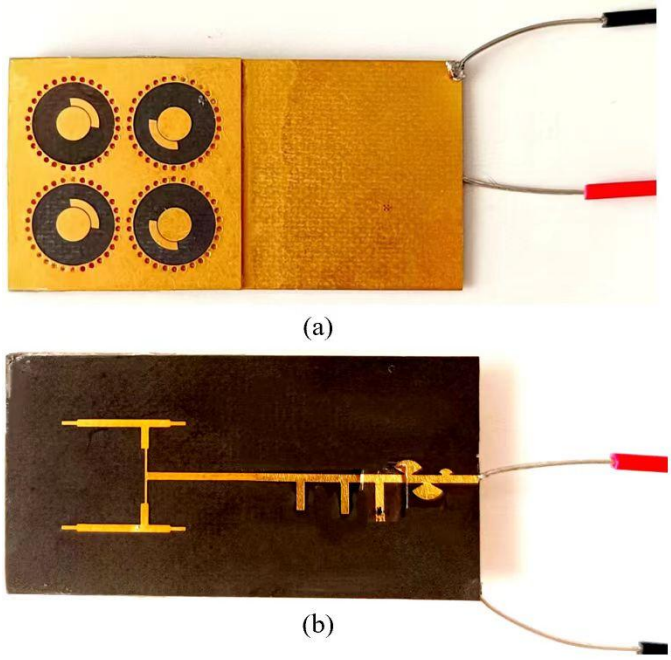

Fig. 21. Photographs of the fabricated DBDS CP rectenna: (a) front view and (b) back view.

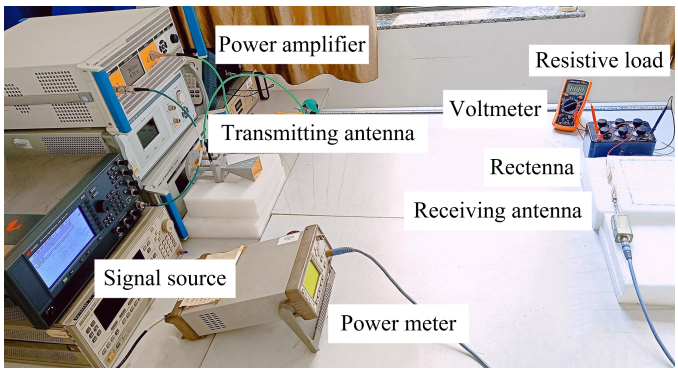

Fig. 22. Measurement setup for the DBDS CP rectenna.

frequency. At 24 GHz, the REs reach maximum values of 40.8% and 48.8% at input powers of 13 dBm and 17 dBm, respectively, to the rectifying circuit. At these powers, the output DC voltages also reach maximum values of 1.91 V and 3.32 V, respectively. As the frequency increases further, the RE and output DC voltage decrease. Similarly, in the frequency range of 26 GHz to 28 GHz, the RE and output DC voltage increase with frequency, reaching maximum values at 28 GHz. At this frequency, the REs are 40.1% and 47.3% at input powers of 13 dBm and 17 dBm, respectively, with corresponding output DC voltages of 1.89 V and 3.27 V. Beyond 28 GHz, the RE and output DC voltage decrease. These results demonstrate that the rectifying circuit exhibits dual-band rectification at 24 GHz and 28 GHz.

The measured RE and the output DC voltage of the rectifying circuit versus the input power are shown in Fig. 20. At 24 GHz and 28 GHz, the output DC voltage increases with input power. At 24 GHz, the RE reaches a maximum value of 50.8% at an input power of 18 dBm, and the output DC voltage reaches a maximum value of 4.63 V at an input power of 20 dBm. At 28 GHz, the RE reaches a maximum value of 49.1% at an input power of 18 dBm, and the output DC voltage reaches a maximum value of 4.51 V at an input power of 20 dBm. The RE is greater than 40% over the input power range of 13 dBm to 20 dBm.

IV. DBDS CP Rectenna Design and Experimental Results

A. DBDS CP Rectenna Structure and Measurement Setup

In this section, we describe the DBDS CP rectenna design and evaluate its performance. The rectenna is formed by integrating the receiving antenna array and the rectifying circuit described in Sections II and III, respectively. Fig. 21 shows photographs of the fabricated DBDS CP rectenna, with physical dimensions of 24 mm × 48 mm × 1.044 mm. Thin copper wires connect the bottom antenna ground and the circuit output to the load.

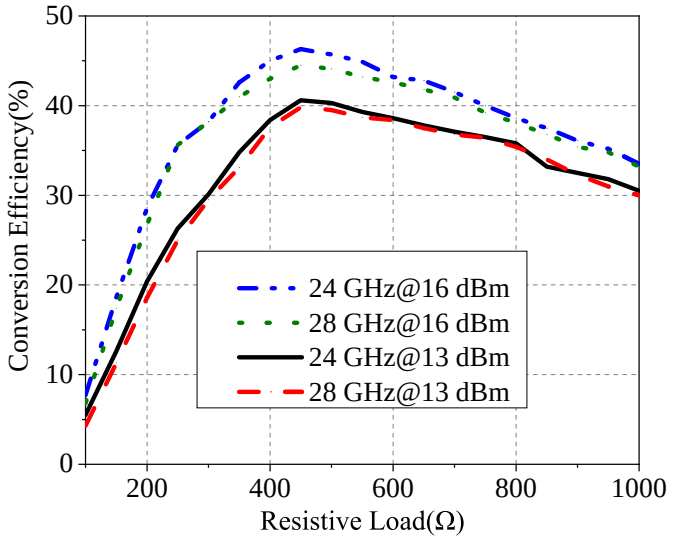

Fig. 23. Measured conversion efficiency of the DBDS CP rectenna versus the load under different input powers.

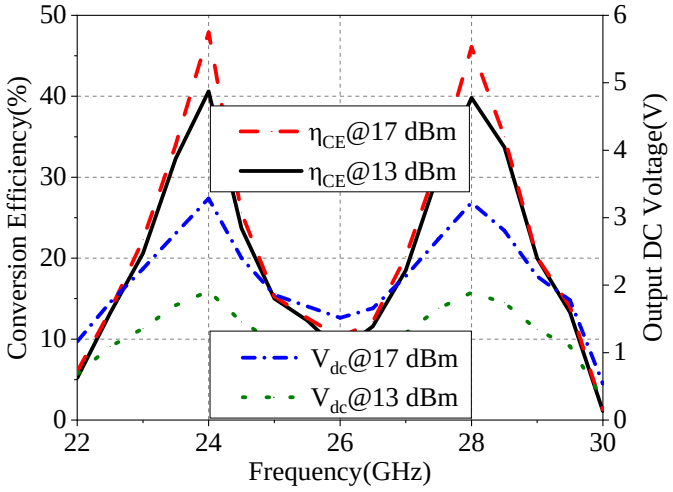

Fig. 24. Measured conversion efficiency and output DC voltage of the DBDS CP rectenna versus frequency under different input powers.

The rectenna's performance is evaluated using the measurement setup shown in Fig. 22. The setup consists of two parts: the transmitting and receiving sections. The transmitting section includes a signal source (Agilent E8257D) that generates linearly polarized signals with a maximum output power of 10 dBm, a power amplifier (Ceyear 3871EB) covering 18 GHz to 30 GHz, and a horn antenna. Since the transmitted signal is linearly polarized, using a misaligned linearly polarized receiving antenna would result in significant polarization mismatch loss, potentially up to 30 dB. In contrast, our CP rectenna inherently mitigates polarization mismatch loss, reducing it to only 3 dB. This is because a CP antenna can equally receive linear polarization components of any orientation. The receiving section comprises the DBDS CP rectenna connected to a resistive load and a voltmeter. The conversion efficiency (CE) of the DBDS CP rectenna is calculated as:

$$\eta_{CE} = \frac{P_{dc}}{P_{in,r}} = \frac{V_{dc}^2}{R_L P_{in,r}} \times 100\%, \tag{9}$$

where P_{dc} is the DC output power of the rectenna, $P_{in,r}$ is the input power to the rectenna, V_{dc} is the DC voltage across the load, and R_L is the resistive load connected to the rectenna.

To precisely determine the input power to the rectenna, $P_{in,r}$, a calibrated receiving antenna is temporarily placed at the same position as the rectenna and connected to a power meter to measure the input power directly, eliminating reliance on the Friis transmission equation. This rectenna measurement setup is applicable in both far-field and near-field conditions.

B. Measurement of the DBDS CP Rectenna

The measured CE of the DBDS CP rectenna versus the load resistance at input powers of 13 dBm and 16 dBm supplied to the rectenna is shown in Fig. 23. At 24 GHz, the CE is 40.6% and 46.3% at input powers of 13 dBm and 16 dBm, respectively, with the highest efficiency at $R_L = 450\Omega$. At 28 GHz, the CE is 39.8% and 44.5% under the same input powers, with the highest efficiency at $R_L = 450\Omega$. This confirms that the optimal load is 450 Ω, consistent with the rectifying circuit design.

The measured CE and the output DC voltage of the DBDS CP rectenna versus the frequency for a 450 Ω resistive load at input powers of 13 dBm and 17 dBm supplied to the rectenna are shown in Fig. 24. In the frequency range of 22 GHz to 24 GHz, both CE and output voltage increase with frequency. At 24 GHz, the CE reaches the highest values of 40.6% and 47.9% for input powers of 13 dBm and 17 dBm, respectively. Moreover, at these powers, the output DC voltages also reach the highest values of 1.9 V and 3.28 v, respectively. As the frequency increases, the CE and output DC voltage decrease. In the frequency range of 26 GHz to 28 GHz, the CE and output DC voltage increase with frequency. At 28 GHz, the CE reaches the highest values of 39.8% and 46.1% at input powers of 13 dBm and 17 dBm, respectively. At these powers, the output DC voltage also reaches maximum values of 1.88 V and 3.22 V, respectively. Then, the CE and output DC voltage decrease as the frequency increases further. These results indicate that the rectenna demonstrates efficient dual-band rectification at 24 GHz and 28 GHz.

The measured CE and output DC voltage of the DBDS CP rectenna versus the input power are shown in Fig. 25. At 24 GHz and 28 GHz, the output DC voltage increases with the input power. Specifically, at 24 GHz, the maximum CE of 49.1% is achieved at an input power of 18 dBm, and the maximum output DC voltage of 4.56 V is achieved at an input power of 20 dBm. At 28 GHz, the maximum CE of 47.8% is obtained at an input power of 18 dBm, and the maximum output DC voltage of 4.46V is achieved at an input power of 20 dBm. The rectenna generally maintains a high CE, which is above 40% across the input power range of 13 dBm to 20 dBm.

To examine the circular polarization performance of the DBDS CP rectenna, the output voltages are measured at different azimuth angles with frequencies of 24 GHz and 28 GHz. For comparison, the output voltages of an LP horn antenna

TABLE III
COMPARISON OF MEASUREMENTS OF THE PROPOSED RECTENNA WITH SIMILAR WORKS

Ref.	Operating Frequency (GHz)	Polarization State	Gain (dBi)	Gain (dBic)	Input Power (dBm)	Conversion Efficiency (%)	Output DC Voltage (V)	Footprint	Thickness
[24]	24	LP	5.0	/	18	/	2.5	/	0.01λ
[25]	24	LP	13.8	/	16	35.0	/	2.1λ × 5.7λ	0.04λ
[26]	24	LP	8.0	/	20	/	6.5	1.3λ × 2.6λ	0.26λ
[27]	24	Dual LP	4.8	/	14	43.0 (sim.)	/	/	/
[3]	24	CP	/	12.6	12.6	42.0	/	/	0.1λ
[5]	24	CP	/	11.3	15.2	63	/	1.6λ × 1.6λ	0.06λ
This work	24/ 28	LHCP/ RHCP	/	17.1/ 17.0	18	49.1/ 47.8	3.7/ 3.6	1.9λ × 3.8λ	0.08λ

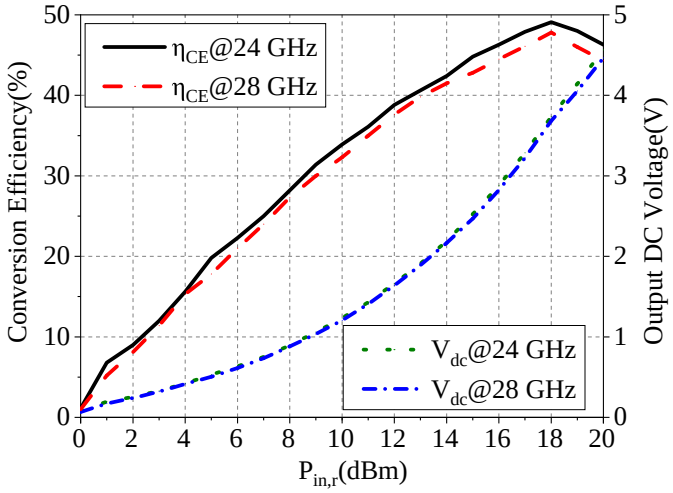

Fig. 25. Measured conversion efficiency and output DC voltage of the DBDS CP rectenna versus input power.

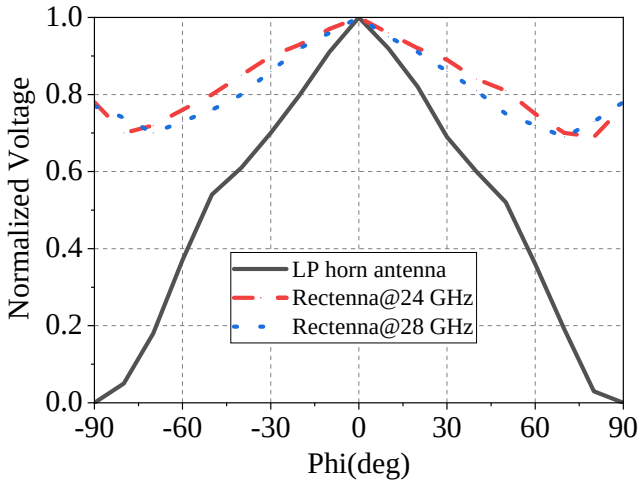

Fig. 26. Normalized output voltages of the DBDS CP rectenna and the LP horn antenna at different angles.

are also evaluated. The measured values are normalized with respect to the output voltage in the 0° direction, as shown in Fig. 26. The results show that when they are rotated by 40°, the normalized voltage of the DBDS CP rectenna is about 0.85, while the normalized voltage of the LP horn antenna is about 0.61. When they are rotated by 90°, the normalized voltage of the DBDS CP rectenna is about 0.78, while the normalized voltage of the LP horn antenna is close to zero.

Finally, the performance of our proposed DBDS CP rectenna is compared with existing rectennas in the literature, including LP rectennas, dual-LP rectennas, and CP rectennas applied in MMPT systems, as summarized in Table III. Our proposed rectenna enables dual-sense circular polarization operation and dual-band rectification in the MMW band, offering higher gains and efficiencies than existing designs.

V. CONCLUSION

In this paper, we proposed and demonstrated the first dual-band dual-sense circularly polarized (DBDS CP) rectenna operating at 24 GHz and 28 GHz for millimeter-wave power transmission. By introducing an arc-shaped parasitic patch near a circular patch to create a chiral structure, we achieved a simple, single-layer design. This chiral structure transforms linearly polarized (LP) waves coupled from a slot into left-hand circularly polarized (LHCP) and right-hand circularly polarized (RHCP) waves at 24 GHz and 28 GHz, respectively. Utilizing substrate-integrated waveguide (SIW) cavities and an array configuration, the receiving antenna array achieves high gains of 17.1 dBic at 24 GHz and 17.0 dBic at 28 GHz.

We also designed an efficient dual-band rectifying circuit using two L-section impedance transformers and three fan-shaped low-pass filters, eliminating the need for lumped components. The integration of the receiving antenna array with the rectifying circuit formed a compact and efficient DBDS CP rectenna, demonstrating high conversion efficiencies of 49.1% at 24 GHz and 47.8% at 28 GHz, both at an input power of 18 dBm. The proposed design features a simple structure with a low profile, facilitating scalability for large-scale arrays in millimeter-wave power transmission applications.

REFERENCES

[1] N. Shinohara, "History and innovation of wireless power transfer via microwaves," *IEEE J. Microw.*, vol. 1, no. 1, pp. 218–228, Jan. 2021.
[2] D. Surender, M. A. Halimi, T. Khan, F. A. Talukdar, and S. R. Rengarajan, "5G/millimeter-wave rectenna systems for radio-frequency energy harvesting/wireless power transmission applications: An overview," *IEEE Antennas Propag. Mag.*, vol. 65, no. 3, pp. 57–76, Jun. 2023.

[3] S. Ladan, A. B. Guntupalli, and K. Wu, "A high-efficiency 24 GHz rectenna development towards millimeter-wave energy harvesting and wireless power transmission," *IEEE Trans. Circuits Syst. I, Reg. Papers*, vol. 61, no. 12, pp. 3358–3366, Dec. 2014.

[4] H. Mei, X. Yang, B. Han, and G. Tan, "High-efficiency microstrip rectenna for microwave power transmission at Ka band with low cost," *IET Microw., Antennas Propag.*, vol. 10, no. 15, pp. 1648–1655, Dec. 2016.

[5] W. Huang, J. Du, X.-X. Yang, W. Che, and S. Gao, "A novel 24 GHz circularly polarised metasurface rectenna," *IET Microw., Antennas Propag.*, vol. 17, no. 6, pp. 419–426, May 2023.

[6] H.-K. Chiou and I.-S. Chen, "High-efficiency dual-band on-chip rectenna for 35- and 94-GHz wireless power transmission in 0.13-μm CMOS technology," *IEEE Trans. Microw. Theory Techn.*, vol. 58, no. 12, pp. 3598–3606, Dec. 2010.

[7] A. Riaz, S. Zakir, M. M. Farooq, M. Awais, and W. T. Khan, "A triband rectifier toward millimeter-wave frequencies for energy harvesting and wireless power-transfer applications," *IEEE Microw. Wireless Compon. Lett.*, vol. 31, no. 2, pp. 192–195, Feb. 2021.

[8] D. Surender, M. A. Halimi, T. Khan, F. A. Talukdar, and Y. M. M. Antar, "A 90° twisted quarter-sectored compact and circularly polarized DR-rectenna for RF energy harvesting applications," *IEEE Antennas Wireless Propag. Lett.*, vol. 21, no. 6, pp. 1139–1143, Jun. 2022.

[9] M. A. Halimi, D. Surender, T. Khan, A. A. Kishk, and S. R. Rengarajan, "A multistepped transmission line matching strategy based triple-band rectifier for RFEH/WPT applications," *IEEE Microw. Wireless Compon. Lett.*, vol. 32, no. 8, pp. 1007–1010, Aug. 2022.

[10] D. Surender *et al.*, "Analysis of facet-loaded rectangular DR-rectenna designs for multisource RF energy-harvesting applications," *IEEE Trans. Antennas Propag.*, vol. 71, no. 2, pp. 1273–1284, Feb. 2023.

[11] J. Heikkinen and M. Kivikoski, "A novel dual-frequency circularly polarized rectenna," *IEEE Antennas Wireless Propag. Lett.*, vol. 2, pp. 330–333, 2003.

[12] Q. Chen, P. Zhao, S. Chen, G. Wang, and X. Chen, "A dual-frequency circularly polarized rectenna for 2.45 and 5.8 GHz wireless power transmission," in *Proc. IEEE Asia–Pacific Conf. Antennas Propag. (APCAP)*, Aug. 2018, pp. 407–409.

[13] J.-D. Zhang, W. Wu, and D.-G. Fang, "Dual-band and dual-circularly polarized shared-aperture array antennas with single-layer substrate," *IEEE Trans. Antennas Propag.*, vol. 64, no. 1, pp. 109–116, Jan. 2016.

[14] H. Yang, Y. Fan, and X. Liu, "A compact dual-band stacked patch antenna with dual circular polarizations for BeiDou navigation satellite systems," *IEEE Antennas Wireless Propag. Lett.*, vol. 18, no. 7, pp. 1472–1476, Jul. 2019.

[15] J.-D. Zhang, L. Zhu, N.-W. Liu, and W. Wu, "Dual-band and dual-circularly polarized single-layer microstrip array based on multiresonant modes," *IEEE Trans. Antennas Propag.*, vol. 65, no. 3, pp. 1428–1433, Mar. 2017.

[16] Y.-K. Jung and B. Lee, "Dual-band circularly polarized microstrip RFID reader antenna using metamaterial branch-line coupler," *IEEE Trans. Antennas Propag.*, vol. 60, no. 2, pp. 786–791, Feb. 2012.

[17] J. B. Pendry, "A chiral route to negative refraction," *Science*, vol. 306, no. 5700, pp. 1353–1355, Nov. 2004.

[18] X. Ma, C. Huang, W. Pan, B. Zhao, J. Cui, and X. Luo, "A dual circularly polarized horn antenna in Ku-band based on chiral metamaterial," *IEEE Trans. Antennas Propag.*, vol. 62, no. 4, pp. 2307–2311, Apr. 2014.

[19] C. Chen, Z.-G. Liu, H. Wang, and Y. Guo, "Metamaterial-inspired self-polarizing dual-band dual-orthogonal circularly polarized Fabry–Pérot resonator antennas," *IEEE Trans. Antennas Propag.*, vol. 67, no. 2, pp. 1329–1334, Feb. 2019.

[20] Y. Wang and X.-X. Yang, "A dual-band dual-sense circularly polarized antenna based on chiral structure," *Microw. Opt. Technol. Lett.*, vol. 65, no. 6, pp. 1747–1754, Jun. 2023.

[21] A. Derneryd, "Analysis of the microstrip disk antenna element," *IEEE Trans. Antennas Propag.*, vol. 27, no. 5, pp. 660–664, Sep. 1979.

[22] S. E. El-Khamy, R. M. El-Awadi, and E.-B. A. El-Sharrawy, "Simple analysis and design of annular ring microstrip antennas," *IEE Proc. H, Microw., Antennas Propag.*, vol. 133, no. 3, pp. 198–202, Jun. 1986.

[23] Y. Wang, X.-X. Yang, G.-N. Tan, and S. Gao, "Study on millimeter-wave SIW rectenna and arrays with high conversion efficiency," *IEEE Trans. Antennas Propag.*, vol. 69, no. 9, pp. 5503–5511, Sep. 2021.

[24] J. Bito, V. Palazzi, J. Hester, R. Bahr, F. Alimenti, P. Mezzanotte, L. Roselli, and M. M. Tentzeris, "Millimeter-wave ink-jet printed rf energy harvester for next generation flexible electronics," in *2017 IEEE Wireless Power Transfer Conference (WPTC)*. IEEE, May 2017, pp. 1–4.

[25] B. T. Malik, V. Doychinov, A. M. Hayajneh, S. A. R. Zaidi, I. D. Robertson, and N. Somjit, "Wireless power transfer system for battery-less sensor nodes," *IEEE Access*, vol. 8, pp. 95 878–95 887, May 2020.

[26] M. Wagih, G. S. Hilton, A. S. Weddell, and S. Beeby, "Broadband millimeter-wave textile-based flexible rectenna for wearable energy harvesting," *IEEE Trans. Microw. Theory Techn.*, vol. 68, no. 11, pp. 4960–4972, Nov. 2020.

[27] S. Trovarello, D. Masotti, M. Aldrigo, M. Modreanu, and A. Costanzo, "Design of a 24-GHz dual-polarized rectenna integrated on silicon," in *2021 51st European Microwave Conference (EuMC)*. IEEE, Apr. 2022, pp. 684–687.

Yan Wang received the M.S. degree in Electromagnetic Field and Microwave Technology from Shanghai Maritime University, Shanghai, China, in 2015, and the Ph.D. degree in Electromagnetic Field and Microwave Technology from Shanghai University, Shanghai, China, in 2023.

She is currently a Postdoctoral Research Assistant with the Department of Mathematics and Information Technology, The Education University of Hong Kong (EdUHK), Hong Kong SAR, China. Her research interests include millimeter-wave power transmission, wireless information and power transfer, millimeter-wave printed antennas, rectifying circuits, and rectenna design.

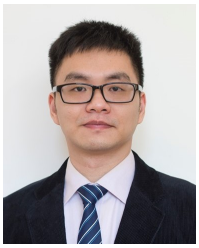

Haoyuan Pan (Member, IEEE) received the B.E. and Ph.D. degrees in Information Engineering from The Chinese University of Hong Kong (CUHK), Hong Kong, in 2014 and 2018, respectively.

He was a Post-Doctoral Fellow with the Department of Information Engineering, CUHK, from 2018 to 2020. He is currently an assistant professor with the College of Computer Science and Software Engineering, Shenzhen University, Shenzhen, China. His research interests include wireless communications and networks, Internet of Things (IoT), semantic communications, and age of information (AoI). He received the Best Paper Award at IEEE Wireless Communications and Networking Conference (WCNC) 2024.

Tse-Tin Chan (Member, IEEE) received his B.Eng. (First Class Hons.) and Ph.D. degrees in Information Engineering from The Chinese University of Hong Kong (CUHK), Hong Kong SAR, China, in 2014 and 2020, respectively.

He is currently an Assistant Professor with the Department of Mathematics and Information Technology, The Education University of Hong Kong (EdUHK), Hong Kong SAR, China. Prior to this, he was an Assistant Professor with the Department of Computer Science, The Hang Seng University of Hong Kong (HSUHK), Hong Kong SAR, China, from 2020 to 2022. His research interests include wireless communications and networking, Internet of Things (IoT), age of information (AoI), and semantic communications.